

Imploding shock wave in a fluid of hard-core particles

P. Gaspard and J. Lutsko

Center for Nonlinear Phenomena and Complex Systems, Université Libre de Bruxelles, Code Postal 231, Campus Plaine, B-1050 Brussels, Belgium

(Received 27 November 2003; revised manuscript received 3 May 2004; published 13 August 2004)

We report the study of a fluid of hard-disk particles in a contracting cavity. Under supersonic contraction speed, a shock wave converges to the center of the cavity where it implodes, creating a central peak in temperature. The dynamics of the fluid is studied by solving the Euler and Navier-Stokes equations, as well as by molecular dynamics simulations and the Enskog direct simulation Monte Carlo method. The value of the maximum temperature reached at the center of the cavity is systematically investigated with the different methods which give consistent results. Moreover, we develop a scaling theory for the maximum temperature based on the self-similar solutions of Euler's equations and mean-free-path considerations. This scaling theory provides a comprehensive scheme for the interpretation of the numerical results. In addition, the effects of the imploding shock wave on a passively driven isomerization reaction $A \rightleftharpoons B$ are also studied.

DOI: 10.1103/PhysRevE.70.026306

PACS number(s): 47.40.Nm, 47.70.Nd, 82.40.Fp, 02.70.Ns

I. INTRODUCTION

In recent years, there has been much interest in the dynamics of collapse of a periodically driven bubble in a liquid [1,2]. Much effort has been devoted to determine the high temperature reached at the center of the bubble at the instant of collapse. The mechanisms studied range from a uniform heating due to adiabatic compression to the implosion of a shock wave if the bubble interface reaches gaseous supersonic speed. This last mechanism has been investigated on the basis of Euler's equations which predicts an infinite temperature at the instant and location the shock wave focuses at the center of the bubble [3]. This infinite temperature is an artifact of Euler's equations which neglect the effects of dissipation due to collisions between the particles in the gas. The simulation of the bubble collapse with the Navier-Stokes equations has shown that the maximum temperature is finite [2,4,5]. Recent molecular dynamics simulations have been carried out which also provide the maximum temperature [1,6,7]. However, no systematic comparison between the continuum and molecular dynamics descriptions exists and little is known analytically about the value of this maximum temperature and its possible effects on chemical reactions.

The purpose of the present paper is to study the maximum temperature reached during the implosion of a shock wave and the induced chemical reaction by molecular dynamics simulations of hard disks in elastic collision in a contracting circular piston. We systematically compare the descriptions based on Euler's equations and the Navier-Stokes equations with molecular dynamics simulations. Molecular dynamics is very appropriate for the study of an imploding shock wave on the scale of the mean free path. In strong planar shocks, the width of the front is indeed known to be of the order of the mean free path. In an imploding shock wave, we should thus expect a smoothing of the discontinuities predicted by Euler's equations on the scale of the mean free path. For our aims, we have therefore carried out a study of the imploding shock wave with molecular dynamics simulations. We consider a hard-disk system which is less time consuming than hard-sphere systems, albeit the scaling properties of an im-

ploding shock wave being qualitatively similar in two and three dimensions. Our principal conclusion is that the hydrodynamic description of the fluid is in good agreement with the molecular dynamics simulations, thus providing support for the use of hydrodynamics to understand the behavior of fluids even under the extreme conditions arising from bubble cavitation.

In typical cavitation conditions, the bubble is periodically driven by the acoustic field and its radius obeys nonlinear equations of the Rayleigh-Plesset type [2,8]. The time dependence of the radius is highly anharmonic, especially, around the time of collapse. The time dependence is determined by the coupling between the gas dynamics inside the bubble and the motion of the surrounding liquid. Studies have shown that spherical bubbles remain stable over a large domain of physical parameters [2,9]. Beside the question of stability, much effort has been devoted to understanding the conditions under which a shock may be generated or not [2,10,11]. In the present paper, our goal is to study a situation with the formation of a shock wave and to understand the saturation of the temperature due to dissipative effects by using molecular dynamics simulations in particular. For this purpose, we may consider a simplified dynamics with a uniformly contracting cavity, ignoring the effects of wall acceleration. Thanks to this simplifying assumption, we can perform a detailed quantitative comparison between the hydrodynamic equations and molecular dynamics simulations, and validate theoretical results about the maximum temperature at collapse.

The paper is organized as follows. In Sec. II, we describe the system we consider and its basic properties such as its equations of states and its transport properties. In Sec. III, the theory of self-similar solutions of Euler's equations is presented, which leads to a theoretical estimation of the maximum central temperature. In Sec. IV, we present the description of the phenomenon in terms of the Navier-Stokes equations. Numerical results of the molecular dynamics simulations are given and discussed in Sec. V. In Sec. VI, we show how an isomerization chemical reaction is induced by

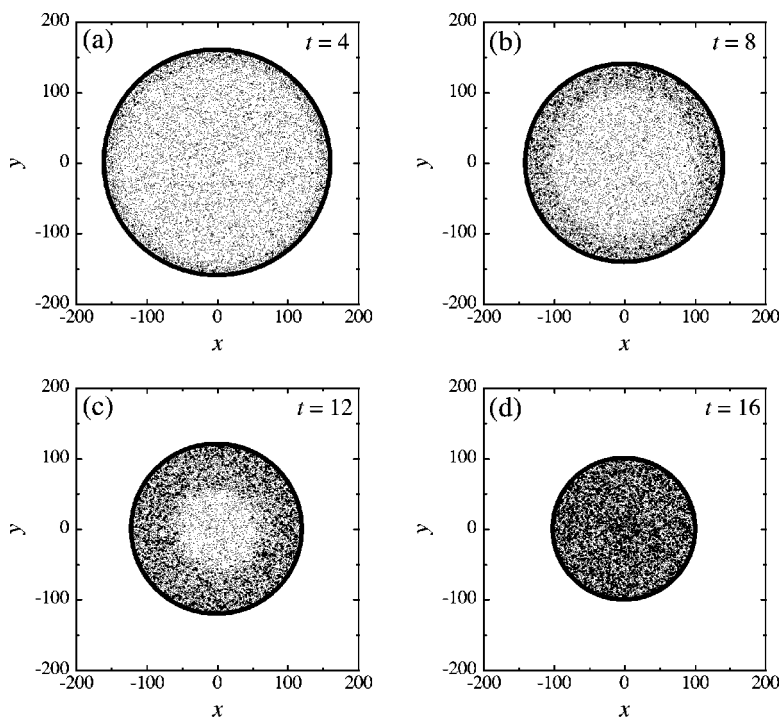


FIG. 1. Time evolution of a fluid of $N = 10\,135$ hard disks of unit mass and diameter in a cavity contracting at the speed $c=5$. We observe the formation of a circular shock wave converging to the center of the cavity. Behind the shock, the heat induces an isomerization $A \leftrightarrow B$ with the activation energy $E_a=50$. The solvent and reactant particles A are depicted as dots and the product particles B appearing behind the shock as disks. Initially, the fluid is at rest with density $n_0=0.1$ and temperature $T_0=1$. The unit of positions x and y is the diameter of the hard disks. The other units are set by taking hard disks of unit mass and $k_B=1$.

heating due to the imploding shock wave. Conclusions are drawn in Sec. VII.

II. DESCRIPTION OF THE SYSTEM

A. System

The system is a fluid of N hard disks inside a circular cavity (or piston) which contracts at a constant speed during some time interval. The radius of the cavity decreases in time according to

$$R(t) = R_0 - ct, \quad \text{for } 0 \leq t < t_f, \quad (1)$$

where the final time t_f is shorter than the time required for the fluid to reach the maximum possible close-packing density for the hard disks. R_0 is the initial radius of the cavity and c is the speed of the wall of the contracting cavity. Figure 1 depicts the time evolution of such a fluid in a contracting cavity and shows the formation of a concentric shock wave converging to the center of the cavity and imploding around time $t \approx 15.5$. Behind the shock front, the density and the temperature jump to higher values than before the front. The heat generated by the shock may induce chemical reactions as shown in Fig. 1. When the shock wave collapses at the center around time $t \approx 15.5$, the temperature culminates at a peak value more than 100 times the initial temperature, while the density is only multiplied by a factor of 4 or less. The purpose of the present paper is to describe quantitatively the implosion of the shock wave and its effects.

B. Dynamics

The N hard disks have masses $\{m_i\}_{i=1}^N$ and radii $\{a_i\}_{i=1}^N$. Their positions and velocities are $\{\mathbf{r}_i\}_{i=1}^N$ and $\{\mathbf{v}_i\}_{i=1}^N$. The

Hamiltonian of the system of hard disks is given by the kinetic energy

$$H = \sum_{i=1}^N \frac{1}{2} m_i \mathbf{v}_i^2. \quad (2)$$

As a consequence, the disks are in free flight between the collisions occurring at times $\{t_n\}$:

$$t_n < t < t_{n+1}: \begin{cases} \mathbf{r}_i(t) = \mathbf{r}_i(t_n) + \mathbf{v}_i^{(+)}(t_n)(t - t_n), \\ \mathbf{v}_i(t) = \mathbf{v}_i^{(+)}(t_n), \end{cases} \quad (3)$$

where $\mathbf{v}_i^{(+)}(t_n)$ is the velocity of disk No. i after the n th collision. We shall denote by $\mathbf{v}_i^{(-)}(t_n)$ the velocity before this collision. The disks are constrained to move in the domain

$$\|\mathbf{r}_i - \mathbf{r}_j\| \geq a_i + a_j, \quad (4)$$

$$\|\mathbf{r}_i\| \leq R(t) - a_i, \quad (5)$$

for $i, j=1, 2, \dots, N$ at all times. These conditions imply that the velocities of both disks i and j involved in a binary collision change according to

$$\begin{aligned} \mathbf{v}_i^{(+)} &= \mathbf{v}_i^{(-)} - 2 \frac{m_j}{m_i + m_j} (\boldsymbol{\epsilon}_{ij} \cdot \mathbf{v}_{ij}^{(-)}) \boldsymbol{\epsilon}_{ij}, \\ \mathbf{v}_j^{(+)} &= \mathbf{v}_j^{(-)} + 2 \frac{m_i}{m_i + m_j} (\boldsymbol{\epsilon}_{ij} \cdot \mathbf{v}_{ij}^{(-)}) \boldsymbol{\epsilon}_{ij}, \end{aligned} \quad (6)$$

where

$$\boldsymbol{\epsilon}_{ij} \equiv \frac{\mathbf{r}_i^{(\pm)} - \mathbf{r}_j^{(\pm)}}{a_i + a_j} \quad (7)$$

is the unit vector joining the centers of the disks and

$$\mathbf{v}_{ij}^{(-)} \equiv \mathbf{v}_i^{(-)} - \mathbf{v}_j^{(-)} \quad (8)$$

is the relative velocity. The positions are unchanged at the instant of the collision: $\mathbf{r}_i = \mathbf{r}_i^{(+)} = \mathbf{r}_i^{(-)}$. Total energy and momentum are conserved during binary collisions.

When a disk collides with the wall of the contracting cavity, it undergoes a specular collision so that its velocity changes according to

$$\mathbf{v}_i^{(+)} = \mathbf{v}_i^{(-)} - 2(\boldsymbol{\epsilon}_i \cdot \mathbf{v}_i^{(-)})\boldsymbol{\epsilon}_i - 2c\boldsymbol{\epsilon}_i, \quad (9)$$

where c is the speed of the wall and

$$\boldsymbol{\epsilon}_i \equiv \frac{\mathbf{r}_i^{(\pm)}}{\|\mathbf{r}_i^{(\pm)}\|} \quad (10)$$

is the unit vector in the direction of the position of disk i from the center of the cavity, which is also, in the cylindrical geometry, the normal to the wall at the point of collision. Total energy and momentum are not conserved during the collision of a particle with the moving wall.

The dynamics (3)–(10) is simulated by an event-driven algorithm based on the redetermination of the next collision after each collision. This algorithm is at the basis of the molecular dynamics simulations of the system.

C. Initial conditions

We consider a fluid of identical particles

$$m_i = m, \quad a_i = a, \quad \text{for all } i = 1, 2, \dots, N, \quad (11)$$

of unit mass $m=1$ and unit diameter $2a=1$.

The initial state of the system is a thermal equilibrium at temperature T_0 and density n_0 when the cavity has the radius $R(t=0)=R_0$. The initial density is therefore

$$n_0 \approx \frac{N}{V_0} = \frac{N}{\pi R_0^2}. \quad (12)$$

The state of thermal equilibrium is obtained during a transient period of equilibration under the molecular dynamics itself while keeping constant the radius of the cavity.

D. Thermodynamics and the equations of state

Here, we use the intensive thermodynamic quantities mass density $\rho=mn$, the specific energy $e=E/M$, and the specific entropy $s=S/M$ where M is the total mass. We suppose that the fluid is locally at equilibrium and that the following local Gibbs relation is satisfied:

$$ds = \frac{1}{T}de + \frac{p}{T}d\frac{1}{\rho}, \quad (13)$$

where p is the local pressure and T the local temperature. We introduce the specific enthalpy as

$$h = e + \frac{p}{\rho}. \quad (14)$$

A fluid of identical particles at equilibrium at the temperature T and density n is characterized by two equations of

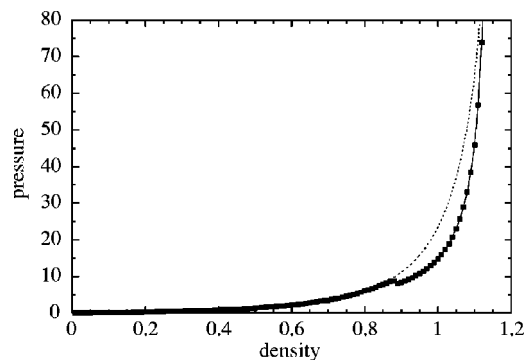


FIG. 2. Pressure p versus density n for a system of 128 hard disks of unit mass and diameter at the temperature $k_B T=1$ calculated numerically by Eqs. (16)–(18) (dots and solid line). The dashed line is the Henderson's empirical equation of state (19) and (20) valid in the fluid phase. The unit of pressure is $k_B T/(2a)^2$ and the unit of density is $1/(2a)^2$ where $2a$ is the diameter of the hard disks.

state. The equation of state for the energy is simply

$$e = \frac{D}{2m}k_B T, \quad \text{with } D=2. \quad (15)$$

(In the numerical calculations, we take units where Boltzmann constant is equal to unity, $k_B=1$.) On the other hand, the equation of state for the pressure is given by

$$p = nk_B T + R, \quad (16)$$

where the rest is calculated with the virial theorem by a time averaging under equilibrium conditions as

$$R = \lim_{V \rightarrow \infty} \left\langle \frac{1}{2VD} \sum_{a \neq b=1}^N \mathbf{F}(\mathbf{r}_{ab}) \cdot \mathbf{r}_{ab} \right\rangle_{\text{eq}} \quad (17)$$

$$= \lim_{V, t \rightarrow \infty} \frac{1}{2tVD} \sum_n \Delta \mathbf{p}_i^{(n)} \cdot \mathbf{r}_{ij}^{(n)} \theta(t - t_n), \quad (18)$$

where D is the dimension, $\mathbf{F}(\mathbf{r}_{ab})$ is the force acting on the particle a due to particle b , $\mathbf{r}_{ab} = \mathbf{r}_a - \mathbf{r}_b$, t_n is the time of the collision between disks i and j , $\Delta \mathbf{p}_i^{(n)} = m[\mathbf{v}_i^{(+)}(t_n) - \mathbf{v}_i^{(-)}(t_n)] = -\Delta \mathbf{p}_j^{(n)}$, and $\mathbf{r}_{ij}^{(n)} = \mathbf{r}_i(t_n) - \mathbf{r}_j(t_n)$. In this way, we have been able to calculate numerically the pressure depicted in Fig. 2.

Since the energy is purely kinetic, the dynamics at different temperatures is the same after a rescaling of time. Hence, the pressure has the form

$$p(T, n) = nk_B T f(y), \quad \text{with } y = \pi a^2 n. \quad (19)$$

For a hard-disk fluid, we use Henderson's empirical equation of state [12]

$$f(y) = \frac{p(T, n)}{nk_B T} = \frac{1 + \frac{y^2}{8}}{(1 - y)^2}. \quad (20)$$

The pressure equation of state can be reexpressed as

$$f(y) = \frac{p(T, n)}{nk_B T} = 1 + 2\pi a^2 n Y(n) = 1 + 2yY(y), \quad (21)$$

in terms of the Enskog factor

$$Y(y) = \frac{1 - \frac{7y}{16}}{(1 - y)^2}. \quad (22)$$

Figure 2 compares the numerical calculation of the pressure with Eqs. (16)–(18) with the analytical expression (19) and (20). The agreement is excellent at low density in the whole fluid phase before the fluid-solid transition.

The system undergoes a fluid-solid transition in the coexistence interval of density $n_f < n < n_s$ with

$$\begin{aligned} \text{fluid-solid transition: } n_f &\approx \frac{0.87 \pm 0.01}{(2a)^2}, \\ n_s &\approx \frac{0.90 \pm 0.01}{(2a)^2}, \end{aligned} \quad (23)$$

independently of the temperature. The pressure diverges at the close-packing density:

$$\text{close-packing density: } n_{cp} = \frac{1}{a^2 2\sqrt{3}} \approx \frac{1.1547}{(2a)^2}, \quad (24)$$

where the hard disks form a perfect triangular lattice.

The specific enthalpy (14) is thus given by

$$h = \frac{k_B T}{m} [1 + f(y)] = \frac{p}{mn} \left[\frac{1}{f(y)} + 1 \right]. \quad (25)$$

The specific entropy of the fluid can be calculated by integrating Gibbs' relation (13) with both equations of states to get

$$s = \frac{k_B}{m} \ln \frac{p}{yf(y) \exp \int \frac{f(y)}{y} dy} + s_*, \quad (26)$$

with a constant of entropy s_* . For the equation of state (20), we obtain the specific entropy

$$s = \frac{k_B}{m} \ln \frac{p(1-y)^{23/8}}{y^2 \left(1 + \frac{y^2}{8}\right) \exp \frac{9}{8(1-y)}} + s_*, \quad (27)$$

which can be rewritten in the form

$$s = \frac{k_B}{m} \ln \frac{p}{y^\gamma \exp C(y)} + s_*, \quad (28)$$

with the exponent $\gamma=2$ and the function

$$\exp C(y) = \frac{1 + \frac{y^2}{8}}{(1-y)^{23/8}} \exp \frac{9}{8(1-y)} = 1 + 4y + O(y^2). \quad (29)$$

The adiabatic is thus given by

$$p = p_* y^\gamma \exp C(y), \quad (30)$$

with the constant of pressure $p_* = \exp[m(s-s_*)/k_B]$.

The sound velocity is given by

$$c_s = \sqrt{\left(\frac{\partial p}{\partial \rho}\right)_s}, \quad (31)$$

where the derivative is taken at fixed entropy, sound being supposed an adiabatic process in first approximation. Accordingly, we obtain

$$c_s^2 = \left(\frac{\partial p}{\partial \rho}\right)_s = \frac{k_B T}{m} \left(f + f^2 + y \frac{df}{dy}\right), \quad (32)$$

with

$$\frac{df}{dy} = 2 \frac{1 + \frac{y}{8}}{(1-y)^3}. \quad (33)$$

For our hard-disk fluid at density $n_0=0.1$ and temperature $T_0=1$, the sound velocity is $c_{s0} \approx 1.66$.

E. Transport properties of the hard-disk fluid

Beside the equilibrium equations of state, the fluid is also characterized by its transport properties which are the shear η and bulk ζ viscosities and the heat conductivity κ . The transport coefficients are given in the Enskog approximation by [13]

$$\eta = \eta_0 b \rho \left(\frac{1}{b \rho Y} + 1 + 0.8729 b \rho Y \right), \quad (34)$$

$$\zeta = \eta_0 b \rho (1.246 b \rho Y), \quad (35)$$

$$\kappa = \kappa_0 b \rho \left(\frac{1}{b \rho Y} + \frac{3}{2} + 0.8718 b \rho Y \right), \quad (36)$$

with

$$b \rho = 2\pi a^2 n = 2y \quad (37)$$

and

$$\eta_0 = \frac{1.022}{4a} \sqrt{\frac{m k_B T}{\pi}}, \quad (38)$$

$$\kappa_0 = \frac{1.029}{a} \sqrt{\frac{k_B^3 T}{m \pi}}. \quad (39)$$

These transport properties arise because the fluid is composed of particles which have the mean free path

$$\ell \approx \frac{1}{4\sqrt{2} a n Y(n)} \quad (40)$$

in a dilute-to-dense hard-disk fluid at equilibrium, where $Y(n)$ is Enskog's factor of the Enskog kinetic theory of dense fluids [14]. The mean free path is the characteristic spatial scale of dissipative and kinetic effects in the fluid.

III. SELF-SIMILAR SOLUTIONS OF EULER'S EQUATIONS

A. Euler's equations

On large scales, a supersonic flow is well described by Euler's equations because dissipation only manifests itself on small scales of the order of the mean free path. In this non-dissipative approximation, the processes are adiabatic—i.e., isentropic—and $ds/dt=0$.

We assume that the flow keeps a rotational symmetry as observed in molecular simulations. Therefore, the velocity macrofield is radial $\mathbf{u}=u\mathbf{e}_r$, and Euler's equations become

$$\partial_t \rho + \partial_r(\rho u) + \frac{D-1}{r} \rho u = 0, \quad (41)$$

$$\partial_t u + u \partial_r u + \frac{1}{\rho} \partial_r p = 0, \quad (42)$$

$$\partial_t s + u \partial_r s = 0, \quad (43)$$

where D is the dimension of space, and the entropy is related to the pressure and the mass density by

$$s = \frac{k_B}{m} \ln \frac{p}{\rho^\gamma \exp C(\rho)} + s'_*. \quad (44)$$

The fluid is not polytropic because $C \neq 0$.

Equations (41)–(43) form a system of three partial differential equations for the three unknown macrofields which are the mass density ρ , the velocity u , and the pressure p . Equation (43) implies that the specific entropy s is locally constant so that the state equation (44) relates the pressure to the mass density.

B. Self-similar solutions

We are looking for self-similar solutions of Eqs. (41)–(44). For polytropic gases, such self-similar solutions have been previously studied [15,16]. However, the problem has to be reformulated because we have here a nonpolytropic fluid, which is a case not treated in Refs. [15,16].

The implosion of the shock wave occurs when $r=0$ at some time $t=t_*$. Thereafter, it reflects on itself and moves outward at times $t > t_*$. Here, we restrict our attention to the period $t < t_*$. We introduce the scaling variable

$$\xi \equiv \frac{r}{A(t_* - t)^\alpha}, \quad (45)$$

with an exponent α to be determined. The converging shock corresponds to the value $\xi=1$; i.e., the front of the shock wave follows the trajectory

$$r_{\text{shock}} = A(t_* - t)^\alpha. \quad (46)$$

We further notice that the time of implosion $t=t_*$ corresponds to $\xi=\infty$.

The macrofields are assumed to be of the form

$$\rho = \rho_0 G(\xi), \quad (47)$$

$$u = \frac{\alpha r}{t - t_*} V(\xi), \quad (48)$$

$$p = \frac{\alpha^2 r^2}{\gamma(t - t_*)^2} G(\xi) Z(\xi), \quad (49)$$

with unknown dimensionless functions $G(\xi)$ for the density, $V(\xi)$ for the velocity, $Z(\xi)$ for the ratio of pressure to density, and ρ_0 a reference density. We notice that the function $Z(\xi)$ in Eq. (49) describes the behavior of the temperature macrofield.

C. Reduction to ordinary differential equations

The self-similar solutions have the mathematical advantage to be expressed in terms of functions depending on the single variable ξ . Therefore, the three partial differential equations reduce to the following three ordinary differential equations in the case of self-similar solutions:

$$\frac{dV}{d \ln \xi} + (V-1) \frac{d \ln G}{d \ln \xi} + DV = 0, \quad (50)$$

$$(V-1) \frac{dV}{d \ln \xi} + \frac{Z}{\gamma} \frac{d \ln G}{d \ln \xi} + \frac{1}{\gamma} \frac{dZ}{d \ln \xi} + \frac{2}{\gamma} Z - V \left(\frac{1}{\alpha} - V \right) = 0, \quad (51)$$

$$(1-\gamma) \frac{d \ln G}{d \ln \xi} + \frac{d \ln Z}{d \ln \xi} - C'(G) \frac{dG}{d \ln \xi} + 2 \frac{\frac{1}{\alpha} - V}{1 - V} = 0, \quad (52)$$

where $C'(G)=dC/dG$. This system of ordinary differential equations can be written in an explicit form. In the case where $D=2$ and $\gamma=2$ which concerns us, we obtain

$$\frac{dV}{d \ln \xi} = \frac{V(V-1) \left(\frac{1}{\alpha} - V \right) + \left[1 - \frac{1}{\alpha} + \left(2 + \frac{C'}{G} \right) V \right] Z}{(V-1)^2 - \left(1 + \frac{C'}{2G} \right) Z}, \quad (53)$$

$$\frac{dZ}{d \ln \xi} = \frac{Z}{1-V} \left\{ -\frac{2}{\alpha} + 2 \left(2 + \frac{C'}{G} \right) V + \left(1 + \frac{C'}{G} \right) \right. \\ \left. \times \frac{V(V-1) \left(\frac{1}{\alpha} - V \right) + \left[1 - \frac{1}{\alpha} + \left(2 + \frac{C'}{G} \right) V \right] Z}{(V-1)^2 - \left(1 + \frac{C'}{2G} \right) Z} \right\}, \quad (54)$$

$$\frac{d \ln G}{d \ln \xi} = \frac{1}{1-V} \times \left\{ 2V + \frac{V(V-1)\left(\frac{1}{\alpha} - V\right) + \left[1 - \frac{1}{\alpha} + \left(2 + \frac{C'}{G}\right)V\right]Z}{(V-1)^2 - \left(1 + \frac{C'}{2G}\right)Z} \right\}, \quad (55)$$

with $C' = C'(G)$.

The solution we are looking for starts from some initial conditions $V(1)$, $Z(1)$, and $G(1)$ determined by the discontinuity of the macrofields along the shock itself, $\xi=1$ or $\ln \xi = 0$. The solution ends at $\xi=\infty$ or $\ln \xi = \infty$ at the origin $V=Z=0$ in the plane (V,Z) . If we linearize Eqs. (53) and (54) around the origin, we obtain around $V \approx 0$ and $Z \approx 0$:

$$\frac{dV}{d \ln \xi} \approx -\frac{V}{\alpha} - \left(\frac{1}{\alpha} - 1\right)Z, \quad (56)$$

$$\frac{dZ}{d \ln \xi} \approx -\frac{2}{\alpha}Z. \quad (57)$$

The solutions of these linearized equations are

$$V \approx \frac{K_V}{\xi^{1/\alpha}}, \quad Z \approx \frac{K_Z}{\xi^{2/\alpha}}, \quad (58)$$

with some constants K_V and K_Z . Equation (58) describes the divergence of the velocity, pressure, and temperature macrofields at the implosion. We notice that the divergence of the temperature Z goes like the square of the divergence of the velocity, as expected by a simple kinematic argument. On the other hand, Eq. (55) for the density reduces at $V \approx 0$ and $Z \approx 0$ to

$$\frac{d \ln G}{d \ln \xi} \approx \left(2 - \frac{1}{\alpha}\right)V + \left(1 - \frac{1}{\alpha}\right)Z \rightarrow 0, \quad (59)$$

so that we can conclude that the density G remains finite at $\xi=\infty$.

The system of ordinary differential equations (53)–(55) is defined in the phase space of the three variables (V,Z,G) . Between the initial conditions $[V(1),Z(1),G(1)]$ and the final conditions $[V(\infty)=0,Z(\infty)=0,G(\infty)]$, the trajectory meets a surface of singularity where Eqs. (53)–(55) diverge. This singularity surface is located where the denominator vanishes:

$$Z = \frac{(V-1)^2}{1 + \frac{C'}{2G}}. \quad (60)$$

On the other hand, this singularity is compensated by the vanishing of the numerator on the null surface:

$$Z = \frac{V(1-V)\left(\frac{1}{\alpha} - V\right)}{1 - \frac{1}{\alpha} + \left(2 + \frac{C'}{G}\right)V}, \quad (61)$$

which intersects the singularity surface (60) along lines in the three-dimensional phase space. The initial conditions are separated from the line $V=Z=0$ of final conditions by both surfaces (60) and (61). For an arbitrary value of α , the trajectory will meet the singularity surface and will not be able to reach the line of final conditions. Nevertheless, there exists a critical value of α to be found numerically such that the trajectory crosses both surfaces on a line at their intersection where Eqs. (53)–(55) are not singular. This critical value of α determines the exponent of the self-similar solution we are looking for.

D. Matching equations

The initial conditions $[V(1),Z(1),G(1)]$ are determined by the matching equations which rule the flow at the discontinuity of the shock wave [15]. In a frame moving with the shock, the matching equations to be satisfied at the discontinuity are

$$\rho_1 u_1 = \rho_2 u_2, \quad (62)$$

$$p_1 + \rho_1 u_1^2 = p_2 + \rho_2 u_2^2, \quad (63)$$

$$h_1 + \frac{u_1^2}{2} = h_2 + \frac{u_2^2}{2}, \quad (64)$$

where the subscript 1 denotes the quantities before the shock and the subscript 2 those after the shock. In a fixed frame, the velocities are

$$v_1 = 0, \quad v_2 = u_2 - u_1, \quad (65)$$

for the converging shock at negative times $t < 0$, because the fluid is initially at rest.

Assuming $p_2 \gg p_1$, Eqs. (62)–(64) are solved to obtain the results that

$$\rho_2 = \rho_1 \left[1 + \frac{2}{f(y_2)} \right], \quad (66)$$

$$p_2 = \frac{\rho_1 u_1^2}{1 + \frac{f(y_2)}{2}}, \quad (67)$$

$$v_2 = -\frac{u_1}{1 + \frac{f(y_2)}{2}}, \quad (68)$$

and

TABLE I. Values of the parameters of the self-similar solutions of Euler's equations for the fluid of hard disks of mass $m=1$ and diameter $2a=1$, versus the initial mass density $\rho_0=mm_0$.

ρ_0	α	$V(1)$	$Z(1)$	$G(1)$	$G(\infty)$	K_V	K_Z
0.0	0.80011	0.66667	0.44444	3.00000	4.55271	0.51173	0.46186
0.01	0.79984	0.65630	0.45114	2.90952	4.36333	0.50278	0.46970
0.05	0.79856	0.61672	0.47275	2.60905	3.74678	0.46849	0.49724
0.1	0.79634	0.57073	0.48999	2.32954	3.19073	0.42834	0.52456
0.2	0.78942	0.48741	0.49968	1.95088	2.46971	0.35515	0.56042
0.3	0.77975	0.41276	0.48478	1.70289	2.02502	0.28998	0.57309
0.4	0.76872	0.34492	0.45190	1.52654	1.72831	0.23230	0.56124
0.5	0.75778	0.28290	0.40574	1.39451	1.52073	0.18199	0.52451
0.6	0.74795	0.22617	0.35003	1.29227	1.37065	0.13887	0.46580
0.7	0.73976	0.17450	0.28811	1.21139	1.25937	0.10246	0.39067

$$u_1 = -\dot{r}_{\text{shock}} = \frac{\alpha r_{\text{shock}}}{t - t_*}. \quad (69)$$

The density before the shock is here the initial density of the fluid at rest, $\rho_1 = \rho_0$. After the shock, the density is given by Eq. (66) at $\xi=1$ so that

$$\rho_2 = \rho_0 G(1) = \rho_1 G(1), \quad (70)$$

where the equation

$$G(1) = 1 + \frac{2}{f\left(\frac{\pi a^2}{m} \rho_0 G(1)\right)}, \quad (71)$$

has to be numerically solved by the Newton-Raphson method to determine the initial value $G(1)$. Immediately after the shock, the velocity is given by

$$v_2 = \frac{\alpha r_{\text{shock}}}{t - t_*} V(1), \quad (72)$$

and the pressure by

$$p_2 = \frac{\alpha^2 r_{\text{shock}}^2}{\gamma(t - t_*)^2} \rho_0 G(1) Z(1). \quad (73)$$

Inserting in Eqs. (67) and (68), we obtain the further initial values

$$V(1) = 1 - \frac{1}{G(1)}, \quad (74)$$

$$Z(1) = \gamma \frac{G(1) - 1}{G(1)^2}. \quad (75)$$

E. Numerical construction of the self-similar solutions

The exponent α and the self-similar solutions can then be obtained numerically for each initial density ρ_0 . The values are given in Table I, where we observe that α is less than unity.

Figure 3 depicts the functions $V(\xi)$, $Z(\xi)$, and $G(\xi)$ for several values of ρ_0 . We observe that we have asymptotic

expansions in powers of $\xi^{-1/\alpha}$. For instance for $\rho_0=0.1$, we find numerically that $\alpha \approx 0.796$ and

$$G(\xi) \approx 3.19 - \frac{0.81}{\xi^{1/\alpha}} + \dots, \quad (76)$$

$$V(\xi) \approx \frac{0.43}{\xi^{1/\alpha}} + \frac{0.14}{\xi^{2/\alpha}} + \dots, \quad (77)$$

$$Z(\xi) \approx \frac{0.52}{\xi^{2/\alpha}} - \frac{0.06}{\xi^{3/\alpha}} + \dots, \quad (78)$$

for $\xi \rightarrow \infty$.

There remains to determine the constant A . The shock starts at the initial time $t=0$ when

$$r_{\text{shock}} = r_{\text{piston}} = R_0. \quad (79)$$

Since the position of the shock is given by Eq. (46), we find that

$$R_0 = A t_*^\alpha. \quad (80)$$

On the other hand, the fluid velocity at the piston must be equal to the speed $-c$ of the piston. Since the fluid velocity is known to be Eq. (48), we get the other result that

$$u = -\frac{\alpha R_0}{t_*} V(1) = -c, \quad (81)$$

which shows that the time of implosion is

$$t_* = \alpha V(1) \frac{R_0}{c}. \quad (82)$$

Inserting this result in Eq. (80), we obtain the constant as

$$A = \frac{R_0}{t_*^\alpha} = R_0 \left[\frac{c}{\alpha V(1) R_0} \right]^\alpha \sim c^\alpha R_0^{1-\alpha}. \quad (83)$$

F. Maximum temperature

According to Eq. (58), the macrofields behave at $t=t_*$ near the center of the cavity as

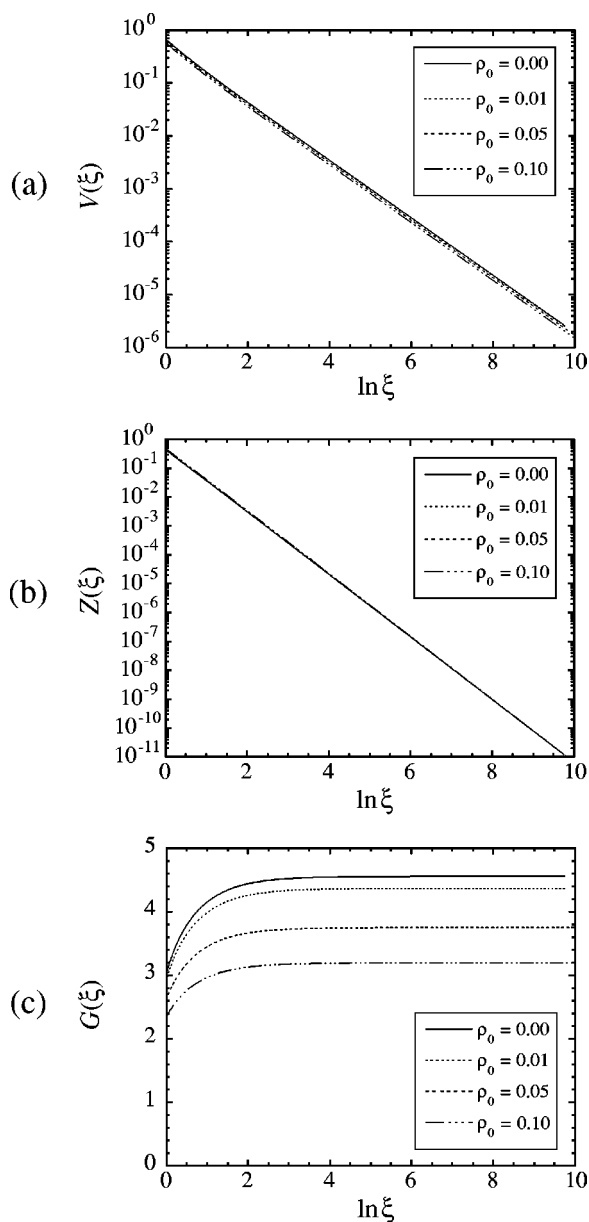


FIG. 3. Self-similar solutions $V(\xi)$, $Z(\xi)$, and $G(\xi)$ of Eqs. (53)–(55) for a fluid of hard disks of unit mass and diameter of initial density $\rho_0 = n_0$ in a contracting cavity. These quantities are dimensionless.

$$\rho \approx \rho_0 G(\infty), \quad (84)$$

$$u \approx \alpha K_V A^{1/\alpha} r^{1-1/\alpha}, \quad (85)$$

$$p \approx \frac{\alpha^2 \rho_0 G(\infty) K_Z}{\gamma} A^{2/\alpha} r^{2-2/\alpha}, \quad (86)$$

for $r \rightarrow 0$. Therefore, we obtain the temperature as

$$k_B T = \frac{p}{n f(y)} \approx \frac{m \alpha^2 K_Z}{\gamma f\left(\frac{\pi a^2}{m} \rho_0 G(\infty)\right)} A^{2/\alpha} r^{2-2/\alpha}, \quad (87)$$

with the constant A given by Eq. (83), whereupon the divergence of the temperature field according to Euler's equations is

$$k_B T = m c^2 \frac{K_Z}{\gamma V(1)^2 f(\pi a^2 n_0 G(\infty))} \left(\frac{R_0}{r}\right)^{(2/\alpha)-2}, \quad (88)$$

for $r \rightarrow 0$, with $f(y) = 1 + 2yY(y)$.

However, this divergence is smoothed out on the scale of the mean free path which is given in Enskog's theory for a hard-disk fluid by

$$\ell(n) \approx \frac{1}{4\sqrt{2}anY(\pi a^2 n)} \quad (D=2), \quad (89)$$

with a density n taking a value in the interval $n_0 < n < n_0 G(\infty)$ between the initial density before the shock and the density after the shock. The density n is thus proportional to n_0 and we consider here the value $n \approx n_0 G(\infty)$ which has been reached at the moment of the implosion.

Finally, the maximum temperature at the center of the cavity is given by

$$k_B T_{\max} \approx m c^2 \frac{K_Z}{\gamma V(1)^2 f[\pi a^2 n_0 G(\infty)]} \left\{ \frac{R_0}{\ell[n_0 G(\infty)]} \right\}^{(2/\alpha)-2}. \quad (90)$$

In $D=2$, we get

$$k_B T_{\max} \approx m c^2 \frac{K_Z}{\gamma V(1)^2 f[\pi a^2 n_0 G(\infty)]} \times \{4\sqrt{2}an_0 G(\infty)Y[\pi a^2 n_0 G(\infty)]R_0\}^{(2/\alpha)-2}. \quad (91)$$

We notice that the exponent α as well as $V(1)$, $G(\infty)$, and K_Z depend on the initial density n_0 in nonpolytropic fluids.

The expression (91) shows that (i) the maximum temperature is independent of the initial temperature T_0 as long as $m c^2 \gg k_B T_0$, (ii) the maximum temperature is proportional to the mass m of the particles, (iii) the maximum temperature is proportional to the square of the speed c of the wall of the contracting cavity, (iv) the maximum temperature scales as $R_0^{(2/\alpha)-2}$ with respect to the initial radius R_0 of the contracting cavity, and (v) in the dilute-gas limit $n_0 \rightarrow 0$, the maximum temperature scales with the initial density n_0 as $n_0^{(2/\alpha_0)-2}$ where $\alpha_0 \approx 0.8$ is the dilute-gas value of the exponent.

As shown in the Appendix, similar results hold in $D=3$ because Eq. (90) also applies to a system in $D=3$ with the corresponding mean free path.

If the fluid is a mixture of particles of different masses $\{m_i\}_{i=1}^s$, the Eulerian description predicts that the molar fractions $x_i = n_i / (\sum_{i=1}^s n_i)$ remain constant in time on a time scale shorter than the time scale of diffusion. As a consequence, the maximum temperature should be proportional to the average mass $m_{\text{av}} = \sum_{i=1}^s x_{i0} m_i$ instead of the mass m in Eq. (90), where x_{i0} are the initial molar fractions.

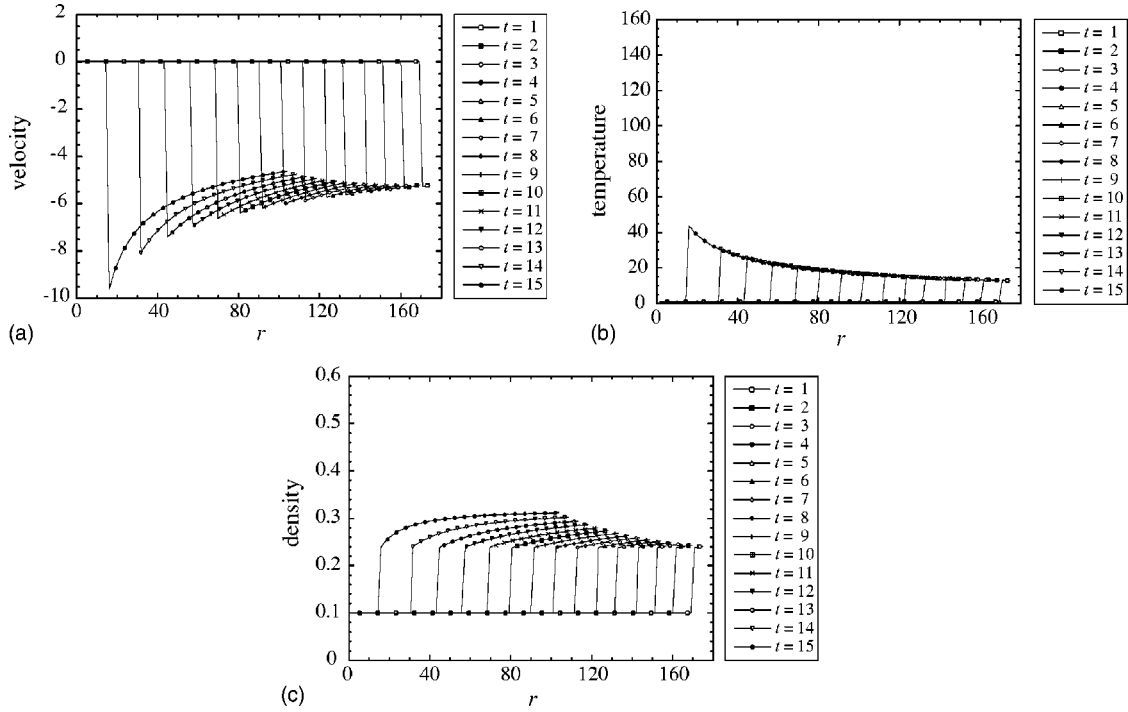


FIG. 4. Profiles of velocity, temperature, and density at successive times t for a fluid at initial density $\rho_0=0.1$ and temperature $T_0=1$ in a contracting cavity of wall velocity $c=5$, according to Euler's equations which ignore dissipation. The units are set by taking hard disks of unit mass and diameter and $k_B=1$.

G. Macrofield profiles versus time

Euler's equations allow us to determine the macrofields of velocity, temperature, and density for a fluid initially at the density $\rho_0=0.1$ in a contracting cavity of wall velocity $c=5$. For this purpose, the self-similar solutions (76)–(78) are used. The result is depicted in Fig. 4. In the Eulerian description, the velocity and temperature blow up to infinity at the center of the cavity at the instant of the implosion. In contrast, the density saturates at a finite value. The shock front propagates according to Eq. (46) with the exponent $\alpha \approx 0.796$. The macrofields are discontinuous at the shock front.

IV. DESCRIPTION BY THE NAVIER-STOKES EQUATIONS

Euler's equations do not take into account the dissipative effects which tend to smooth the front of the shock wave and lead to a saturation of the temperature at implosion. In order to investigate these effects, we have solved the Navier-Stokes equations in a radial geometry. It is known that the Navier-Stokes equations are able to describe the profile of a shock wave in the limit of a weak shock [15]. As we shall see in the following, the Navier-Stokes equations allow us to obtain values for the maximum temperature which are in excellent agreement with the molecular dynamics simulations.

The radially symmetric Navier-Stokes equations are

$$\partial_t \rho + \partial_r(\rho u) + \frac{D-1}{r} \rho u = 0, \quad (92)$$

$$\begin{aligned} \rho(\partial_t u + u \partial_r u + \partial_r p) &= \left(\zeta + 2 \frac{D-1}{D} \eta \right) \partial_r \left(\partial_r u + \frac{D-1}{r} u \right) + \left(\partial_r \zeta \right. \\ &\quad \left. - \frac{2}{D} \partial_r \eta \right) \left(\partial_r u + \frac{D-1}{r} u \right) + 2 \partial_r \eta \partial_r u, \end{aligned} \quad (93)$$

$$\begin{aligned} \rho(\partial_t e + u \partial_r e) + \rho p \left(\partial_r u + \frac{D-1}{r} u \right) &= \frac{1}{r^{D-1}} \partial_r (r^{D-1} \kappa \partial_r T) \\ &\quad + 2 \eta \left[(\partial_r u)^2 + \frac{D-1}{r^2} u^2 \right] + \left(\zeta - \frac{2}{D} \eta \right) \left(\partial_r u + \frac{D-1}{r} u \right)^2, \end{aligned} \quad (94)$$

for the mass density ρ , the fluid velocity u , and the temperature T . For a fluid of hard disks, the specific energy e is related to the temperature T by the equation of state (15), while the pressure p is given by the other equation of state (20). The shear and bulk viscosities (η and ζ) as well as the heat conductivity κ are given by Eqs. (34)–(36).

We have integrated the Navier-Stokes equations for a contracting cavity with a wall moving at speed c . The first possible comparison is with the motion of the shock which can be localized as the point of maximum pressure gradient. Figure 5 shows the position of the imploding shock versus time and we observe good agreement with the scaling (46) predicted by the similarity solution to the Euler equations. Here, the fitted power is $\alpha_{NS} \approx 0.78$ in excellent agreement with the prediction $\alpha \approx 0.796$.

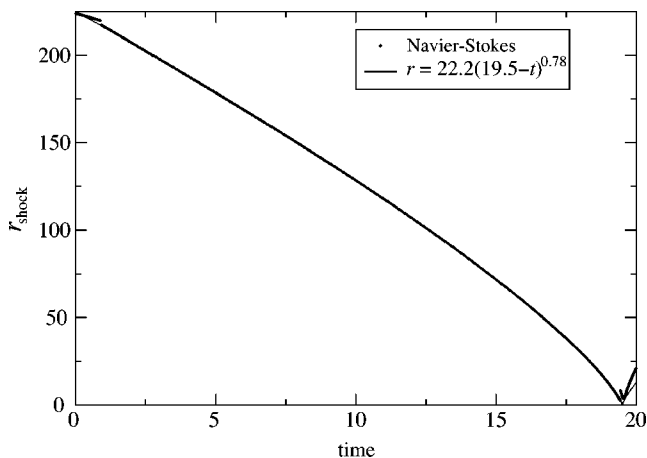


FIG. 5. Propagation of the shock wave in the radial coordinate r versus time, according to the Navier-Stokes equations (dots), for a fluid of initial density $n_0=0.1$ and temperature $T_0=1$. The wall of the circular cavity contracts at the speed $c=5$ from the initial radius $R_0=224$. The implosion happens at the time $t_* \approx 19.5$. The solid line is a fit with the exponent $\alpha_{NS}=0.78$. The units are set by taking hard disks of unit mass and diameter and $k_B=1$. The small discontinuities are artifacts of the algorithm used to track the position of the shock, which is not well defined in the beginning and during reflection at the center.

Figure 6 depicts the temperature macrofield versus time and shows the steep increase of temperature at the center at the moment of the implosion. However, contrary to the prediction of Euler's equations the temperature is not infinite but reaches a maximum, as predicted by our equation (90). Comparing the Navier-Stokes results in Fig. 6 with the Eulerian prediction of Fig. 4(b), we observe that the shock has a nonzero width according to the Navier-Stokes equations. Moreover, the temperature profiles at successive times do not superpose in the Navier-Stokes description although they do so in the Eulerian description. The reason is that the dissipa-

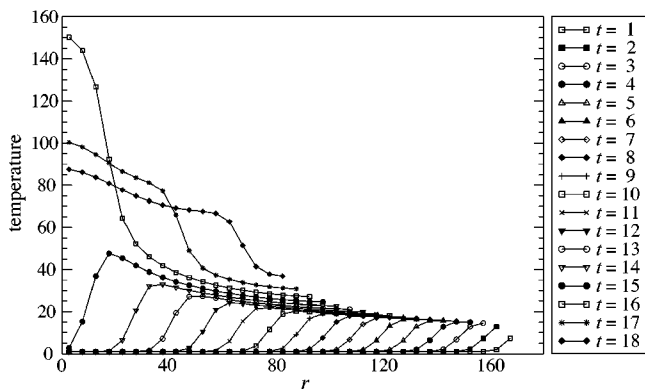


FIG. 6. Time evolution of the temperature macrofield according to the Navier-Stokes equations for a fluid of initial density $n_0=0.1$ and temperature $T_0=1$ in a circular cavity contracting at speed $c=5$ from the initial radius $R_0=180.1$. The implosion happens at the time $t_* \approx 15.5$. We observe that, thereafter, the shock wave propagates outward and bounces back on the wall of the cavity which continues to contract. The units are set by taking hard disks of unit mass and diameter and $k_B=1$.

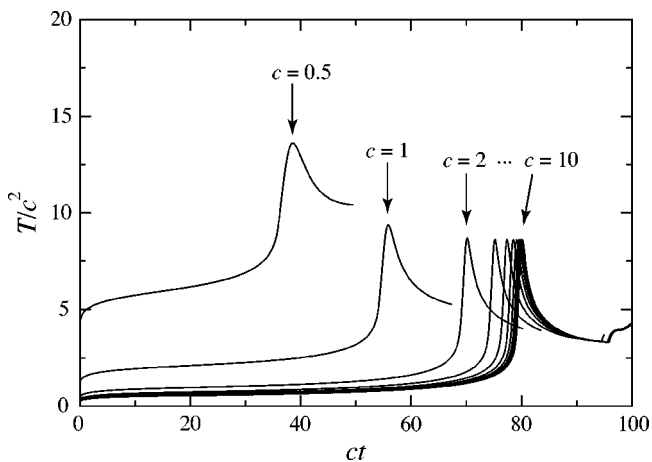


FIG. 7. Central temperature T/c^2 versus time ct , both rescaled by the speed velocity c of the circular wall of the contracting cavity starting from $R_0=180.1$, according to the Navier-Stokes equations for a fluid of initial density $n_0=0.1$ and temperature $T_0=1$, and for different speeds $c=0.5, 1, 2, 3, 4, 5, 6, 7, 8, 9, 10$. The sound velocity of the initial fluid is $c_{s0} \approx 1.66$, which marks the transition between the subsonic and supersonic regimes. The units are the same as in Figs. 5 and 6.

tion included in the Navier-Stokes description continues to heat up the fluid behind the shock due to the viscosities and the heat conductivity, although these dissipative effects are not taken into account in Euler's equations.

In Fig. 7, we have plotted the rescaled central temperature T/c^2 versus the rescaled time ct for cavities contracting at different speeds c . We observe how the temperature increases to a maximum in each case. As $c \rightarrow \infty$, the rescaled curves tend to superpose as expected because we approach the limit where the shock is well described by Euler's equations. In particular, the superposition of the curves is evidence that the maximum temperature scales as c^2 as predicted by Eq. (90). We also observe that for a subsonic speed $c=0.5$ the curve differs from the other curves. Figure 8 confirms that the shock is sharper and sharper as c increases because its width

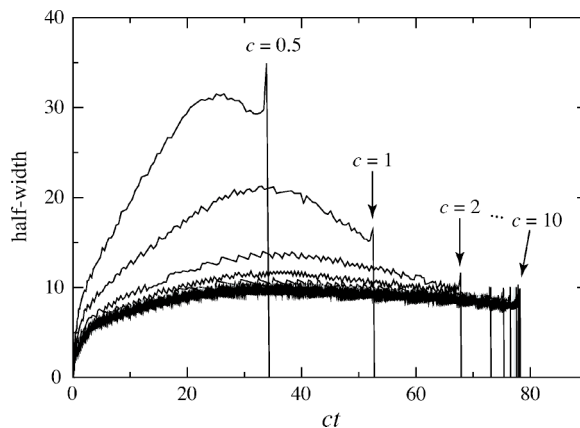


FIG. 8. Half-width of the shock wave versus the rescaled time ct for different contraction speeds $c=0.5, 1, 2, 3, 4, 5, 6, 7, 8, 9, 10$ according to the Navier-Stokes equations with the same conditions and units as in Fig. 7.

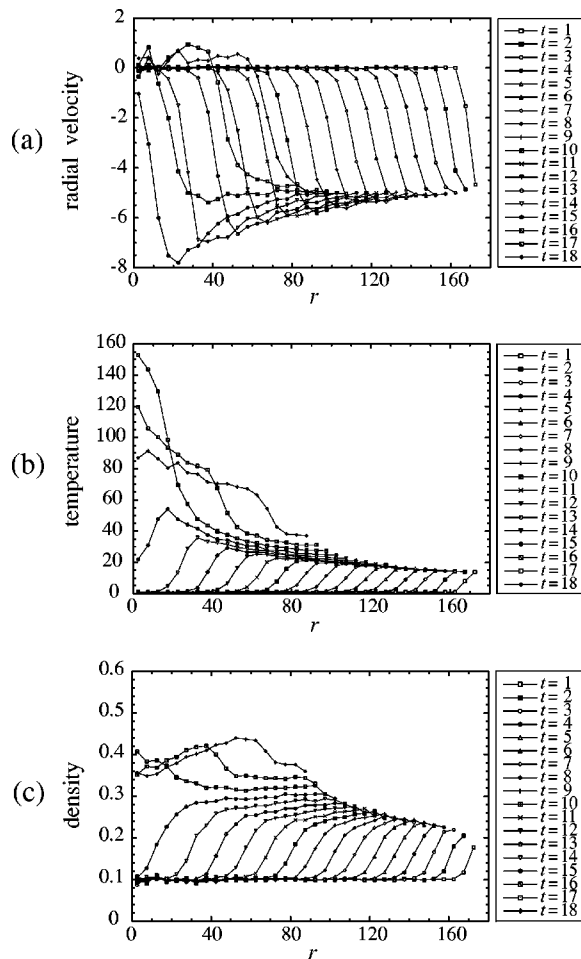


FIG. 9. Molecular dynamics simulations of a fluid of $N = 10135$ hard disks of unit mass and diameter in a circular cavity contracting at speed $c=5$ from an initial radius $R_0=180.1$. Initially the fluid is at rest with initial density $n_0=0.1$ and temperature $T_0 = 1$: (a) profiles of the radial velocity at successive times t versus the radial coordinate r , (b) the same for the temperature macrofield, and (c) the same for the density macrofield. The macrofields are obtained by averaging in concentric annuli of width $\Delta r=5$ using the $10N=101350$ particles of 10 runs. The units are set by taking hard disks of unit mass and diameter and $k_B=1$.

decreases and tends to a value which is of the order of the mean free path. At subsonic speed, we no longer have a shock but instead a broad front.

V. MOLECULAR DYNAMICS SIMULATIONS

The dynamics in a contracting cavity has first been simulated by molecular dynamics simulations by an event-driven algorithm. Figure 9 depicts the velocity, temperature, and density macrofields versus time as calculated by averaging the microscopic quantities over concentric annuli, as well as over ten runs of the full dynamics from different initial conditions of a fluid at rest, at initial density $n=0.1$ and temperature $T=1$. Comparing these results of molecular dynamics with the Eulerian description in Fig. 4, we first of all notice the remarkable similarity. In particular, the time evolution of

the velocity and density macrofields are already very well described by Euler's equations. However, upon closer inspection, differences are noticeable. The molecular dynamics simulations show that the shock wave has a width. Moreover, the temperature at the center of the cavity at the instant of implosion $t_* \approx 15.5$ reaches a finite maximum value at about $T \approx 150$. Besides, the temperature continues to increase behind the shock. This is evidenced by the upward shift of the temperature profiles in Fig. 9(b), though it is not the case in Fig. 4(b). All these features are due to the dissipation which is not taken into account in the Eulerian description. The comparison of the temperature profiles in Fig. 9(b) with those of Fig. 6 given by the integration of the Navier-Stokes equations shows the excellent agreement. This agreement is an evidence that the three aforementioned features can be explained by the Navier-Stokes equations and are therefore the consequences of the dissipation due to the viscosities and the heat conductivity.

The propagation of the shock can be observed for each macrofield in Fig. 9. Using the loci of maximum gradient of each macrofield to define the position of the shock, we can determine its trajectory in Fig. 10 where we observe the near coincidence of the shock position using the different macrofields. Figure 10 shows the remarkable agreement of the power law predicted by the Eulerian self-similar solutions (46) with the molecular dynamics. This result confirms that the propagation of the shock wave is already remarkably well described by Euler's equations, which capture the phenomenon in a very good first approximation. However, dissipative effects are present which requires the Navier-Stokes equations to be described.

Figure 11(a) depicts the central temperature versus time for ten individual runs of the molecular dynamics, as well as their average. After the implosion of the shock wave, the temperature increases to its maximum. Important fluctuations affect the value of the central temperature which can be defined by averaging over different realizations from random initial conditions. Figure 11(b) shows the very good agreement of the central temperature with the result of the integration of Navier-Stokes equations.

We have also simulated the time evolution using the Enskog DSMC method (i.e., direct simulation Monte Carlo method based on Enskog kinetic equation [17]). This stochastic method is in superb agreement with the molecular dynamics. Figure 12 shows the trajectory of the shock obtained using the DSMC method, which scales with the exponent $\alpha_{\text{DSMC}} \approx 0.77$ in agreement with the predicted power law $\alpha \approx 0.796$. The agreement is also excellent with the trajectory calculated by using the Navier-Stokes equations and depicted in Fig. 5 for the same conditions as in Fig. 12.

Finally, the maximum temperature as a function of the initial radius R_0 is depicted in Fig. 13 for the different calculations with the Navier-Stokes equations, the Enskog DSMC method, and the molecular dynamics (MD). Our scaling law (90) predicts a power $\nu = (2/\alpha) - 2 = 0.51 - 0.56$ for $\alpha = 0.796 - 0.780$ depending on whether the density to consider is the density $n=0.1$ before the shock or the density $n \approx 0.3$ at the implosion. We observe in Fig. 13 reasonable agreement of this prediction with the results of different calculations. The power obtained by fits has the value ν_{num} .

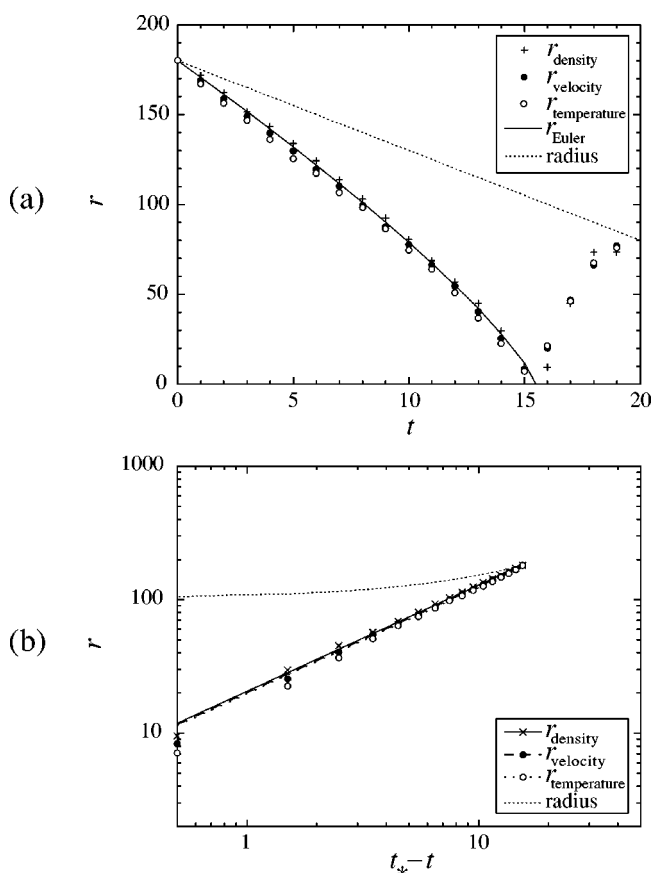


FIG. 10. Propagation of the shock front in a fluid of $N = 10\,135$ hard disks of unit mass and diameter in a circular cavity contracting at speed $c=5$ from an initial radius $R_0=180.1$. Initially the fluid is at rest with initial density $n_0=0.1$ and temperature $T_0 = 1$. The radial position r of the front is determined by the radial coordinate of the steepest gradient of the macrofields in Fig. 9. (a) Radial position r of the shock front versus time. (b) Same as in (a) but in the log-log plot of the radial position r versus the time $t_* - t$ counted with respect to the collapse time t_* in order to display the Eulerian scaling with exponent $\alpha \approx 0.796$ (lines). The units are the same as in Fig. 9.

$=0.59-0.60$ which is slightly higher than the prediction. A reason could be that the scaling law results from an assumption on the value of the density which changes during the process. A complete theory should be based on the asymptotic resolution of the Navier-Stokes equations around Eulerian self-similar solutions. Given the limitations of the present theory, we think that the agreement with the prediction is reasonably good.

The conclusion here is that the dissipative effects are very well described already by the Navier-Stokes equations which allow us to calculate the maximum temperature at implosion in good agreement with the MD and Enskog DSMC results. The theory based on the Eulerian self-similar solutions and mean-free-path considerations provides a comprehensive scheme for understanding the numerical results.

Remark: The molecular dynamics simulations of a binary mixture show that the molar fractions of species of different masses remain unchanged during the short time interval of

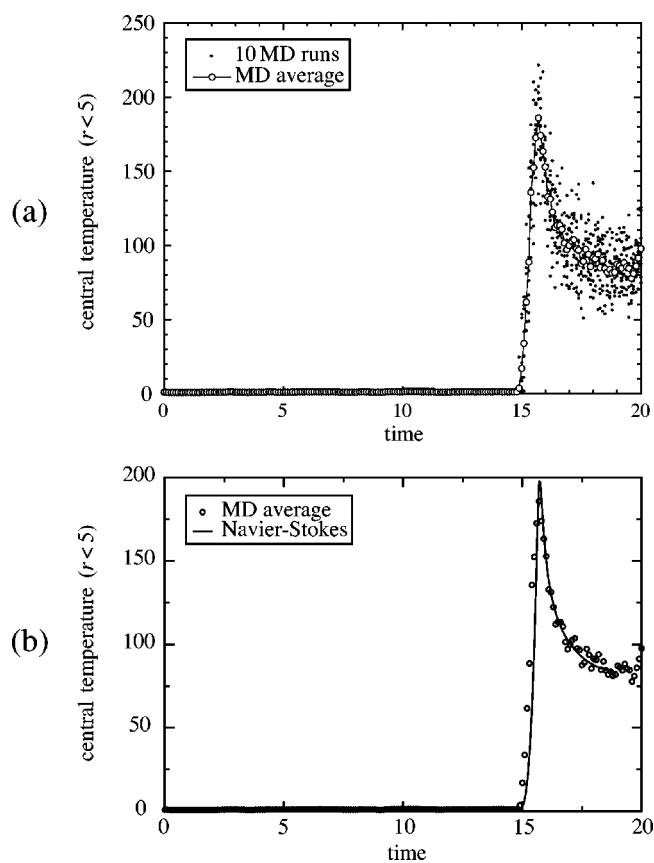


FIG. 11. Time evolution of the central temperature in a fluid of $N=10\,135$ hard disks of unit mass and diameter in a circular cavity contracting at speed $c=5$ from an initial radius $R_0=180.1$. Initially the fluid is at rest with initial density $n_0=0.1$ and temperature $T_0 = 1$. The central temperature is calculated by averaging the kinetic energies of the hard disks in a circle of radial coordinate $0 < r < 5$. (a) Molecular dynamics simulations of the central temperature for ten individual runs (dots) and their average (open circles connected by a line). (b) Comparison between the MD average values (open circles) with the result of the integration of the Navier-Stokes equations (solid line). The units are the same as in Figs. 5–10.

the shock-wave implosion in agreement with the theoretical prediction of Sec. III F.

VI. ISOMERIZATION CHEMICAL REACTION

The reaction we consider is an isomerization between two species $A \rightleftharpoons B$ in the solvent S and without heat exchange so that there is no feedback of the reaction on the hydrodynamics. This reaction is thus passively driven by the hydrodynamics. The advantage is that the reaction acts as a probe of the hydrodynamics. Moreover, it allows us to understand the effects of the coupling between the hydrodynamics and a reaction essentially preserving the energy and the total number of particles.

The reaction is supposed to occur with probability $0 \leq P \leq 1$ if the center-of-mass energy is higher than an activation energy, which means that the reactive cross section is constant above the threshold E_a . The reaction scheme is



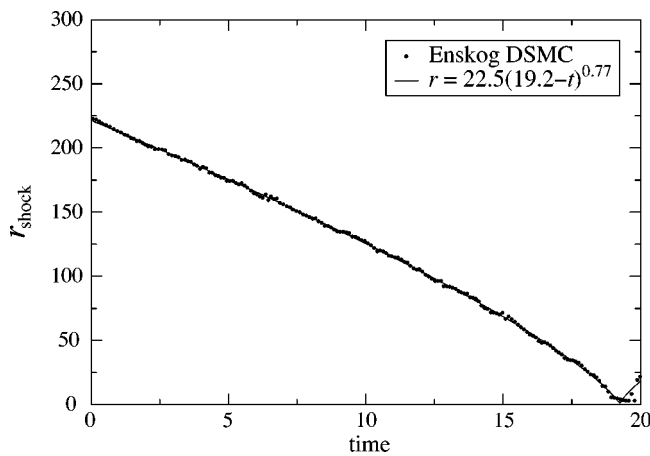


FIG. 12. Simulations with the Enskog DSMC method of the propagation of the shock wave in a fluid of initial density $n_0=0.1$ and temperature $T_0=1$ in a circular cavity contracting at speed $c=5$ from an initial radius $R_0=224$ in the same conditions as in Fig. 5. The implosion happens at time $t_* \approx 19.3$ and the trajectory of the shock front scales with the exponent $\alpha_{\text{DSMC}} \approx 0.77$. The units are the same as in Fig. 5.

$$A + S \rightarrow A + S, \quad E < E_a \vee \{E > E_a \wedge \text{prob. } (1 - P)\}, \quad (96)$$

$$A + S \rightarrow B + S, \quad E > E_a \wedge \text{prob. } P, \quad (97)$$

$$B + S \rightarrow B + S, \quad E < E_a \vee \{E > E_a \wedge \text{prob. } (1 - P)\}, \quad (98)$$

$$B + S \rightarrow A + S, \quad E > E_a \wedge \text{prob. } P, \quad (99)$$

$$A + A \rightarrow A + A, \quad E < E_a \vee \{E > E_a \wedge \text{prob. } (1 - 2P)\}, \quad (100)$$

$$A + A \rightarrow A + B, \quad E > E_a \wedge \text{prob. } P, \quad (101)$$

$$A + A \rightarrow B + A, \quad E > E_a \wedge \text{prob. } P, \quad (102)$$

$$B + B \rightarrow B + B, \quad E < E_a \vee \{E > E_a \wedge \text{prob. } (1 - 2P)\}, \quad (103)$$

$$B + B \rightarrow A + B, \quad E > E_a \wedge \text{prob. } P, \quad (104)$$

$$B + B \rightarrow B + A, \quad E > E_a \wedge \text{prob. } P, \quad (105)$$

$$A + B \rightarrow A + B, \quad E < E_a \vee \{E > E_a \wedge \text{prob. } (1 - 2P)\}, \quad (106)$$

$$A + B \rightarrow A + A, \quad E > E_a \wedge \text{prob. } P, \quad (107)$$

$$A + B \rightarrow B + B, \quad E > E_a \wedge \text{prob. } P, \quad (108)$$

where \vee stands for “or” and \wedge for “and.”

We introduce the concentration difference

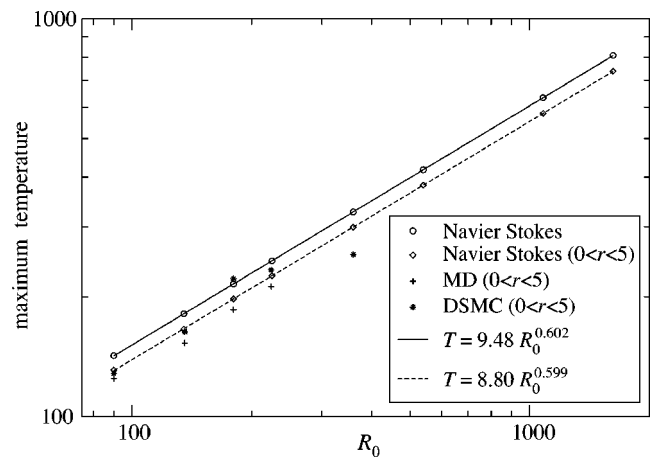


FIG. 13. Compilation of our numerical data for the maximum temperature at the center of the cavity at the instant of implosion versus the initial radius R_0 of the cavity. Initially, the fluid of hard disks is at rest with the density $n_0=0.1$ and the temperature $T_0=1$. The speed of the wall of the contracting cavity is $c=5$. The crosses are the data from the molecular dynamics simulations (MD), the stars from the Enskog DSMC method, the open circles from the Navier-Stokes equations, and the diamonds from the Navier-Stokes equations but with an average of the temperature macrofield over $0 < r < 5$. The reason is that we compare with the MD and DSMC data where the temperature is calculated by averaging the kinetic energies of the particles in $0 < r < 5$. The solid line is a fit to the Navier-Stokes data. The dashed line is a fit to the Navier-Stokes data averaged over $0 < r < 5$. The power-law exponents of the MD and DSMC data are: $\nu_{\text{MD}}=0.59 \pm 0.07$ and $\nu_{\text{DSMC}}=0.52 \pm 0.20$. The units are the same as in Figs. 5–12.

$$c = \frac{m}{\rho}(n_A - n_B), \quad (109)$$

for which the equation of evolution is

$$\partial_t c + u \partial_r c = -2k_+(\rho, T) \frac{\rho}{m} c, \quad (110)$$

with $\rho = m(n_S + n_A + n_B)$. The reaction rate k_+ can be calculated using Enskog kinetic theory [13,14] for the above reaction as

$$k_+ = 8PaY(n) \left[\sqrt{\frac{E_a}{m}} e^{-E_a/k_B T} + \sqrt{\frac{\pi k_B T}{4m}} \text{erfc} \left(\sqrt{\frac{E_a}{k_B T}} \right) \right], \quad (111)$$

where P is the reaction probability, a the disk radius, E_a the activation energy, and $Y(n)$ is Enskog’s factor given here above by Eq. (22). The validity of the kinetic result (111) has been checked in the absence of hydrodynamics by molecular dynamics simulations with an immobile wall of speed $c=0$. Figure 14 shows good agreement with theory.

The reaction has been simulated in a contracting cavity, as depicted in Fig. 1. The initial condition contains only solvent S particles and reactant A particles, so that the products are the B particles. We observe that the B particles are produced behind the shock after heating by the shock. There is no significant reaction within the shock itself. Figure 15(a) de-

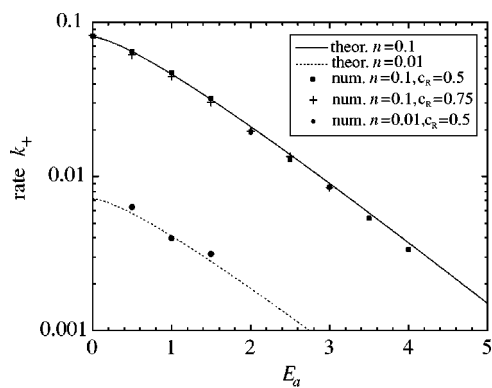


FIG. 14. Reaction rate k_+ versus the activation energy E_a for different mass densities ρ and reactant fractions $c_R=(n_A+n_B)/(n_S+n_A+n_B)$. The dots and crosses are the results of the molecular dynamics simulations while the lines are given by Eq. (111) resulting from Enskog's theory. The simulations are carried out in a fluid of hard disks of unit mass and diameter in elastic and reactive collisions in a circular cavity of constant radius $R=180.1$. The temperature is $T=1$ and the reaction probability $P=0.1$. The units are set by taking hard disks of unit mass and diameter and $k_B=1$.

picts the concentration c_B of products as a function of time calculated using Euler's self-similar solutions. We already see that the products accumulate behind the shock due to the heating, but the rate is lower than it should be because the heating is underestimated by Euler's equations. Figure 15(b) depicts the result with the Navier-Stokes equations coupled to Eq. (110) and a better agreement is obtained with the molecular dynamics simulations [see Fig. 15(c)]. Indeed, we observe that the increase of the concentration c_B behind the shock wave is somewhat larger in the molecular dynamics simulations and the Navier-Stokes calculations than according to the Eulerian description. Here, we see the effects of the heating that we have already observed for the temperature in Figs. 6 and 9(b) due to the viscosities and the heat conductivity. We notice that, at the end of the contraction, the temperature has become so high with respect to the activation energy that an equilibrium has been reached between the A and B particles so that the concentration of the B particles reaches its equilibrium value $c_B=\frac{1}{4}$ for $c_R=\frac{1}{2}$.

VII. CONCLUSIONS

In the present paper, we have studied the formation of a shock wave and its implosion in a circular cavity contracting at a supersonic speed. As a vehicle of our study, we have considered a two-dimensional system of hard disks because it can be efficiently simulated by molecular dynamics using an event-driven algorithm with about $N \approx 10^4$ particles. (In $D=3$, a comparable simulation would require $N \approx 10^6$ particles, which is very much more time consuming.) The advantage to work in $D=2$ is thus a gain in CPU time albeit the properties of the $D=2$ and $D=3$ systems are very similar. For instance, the scaling exponent of the Eulerian self-similar solutions remain in the interval $0 < \alpha < 1$ in both $D=2$ and $D=3$. Therefore, the results in $D=2$ can be extrapolated to $D=3$. We notice that long-time tail effects on the transport

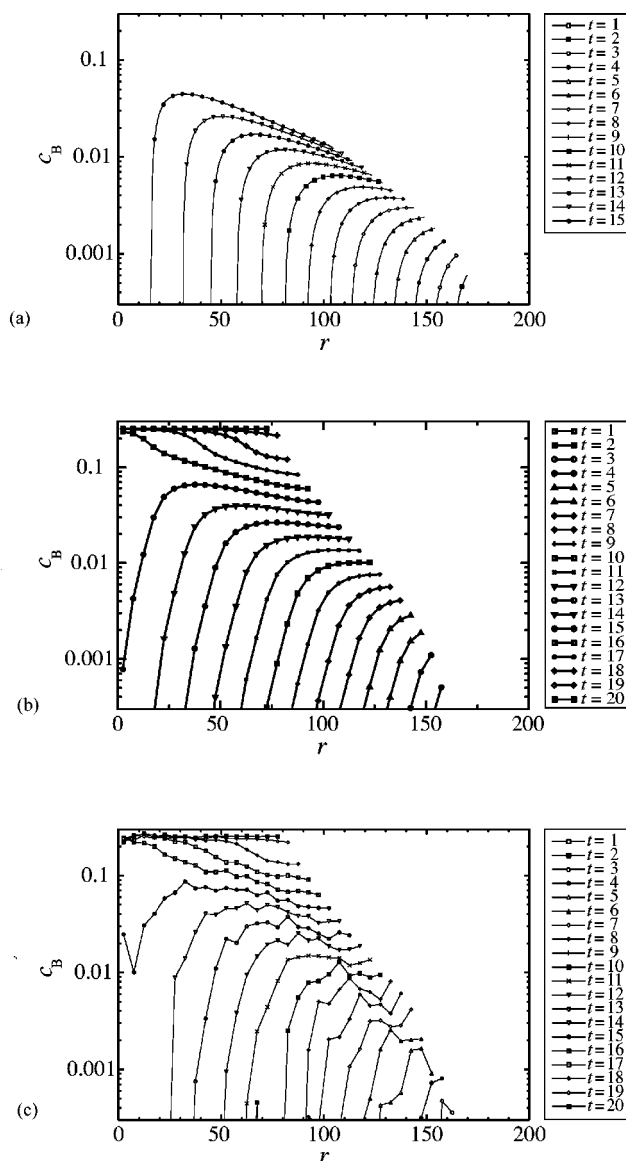


FIG. 15. Time evolution of the concentration c_B of product B particles in a fluid of $N=101\ 35$ hard disks of unit mass and diameter in a circular cavity contracting at speed $c=5$ from an initial radius $R_0=180.1$. Initially the fluid is at rest with initial density $n_0=0.1$ and temperature $T_0=1$ and it contains solvent S particles in the concentration $c_S=\frac{1}{2}$ and reactant A particles in the initial concentration $c_{A0}=\frac{1}{2}$. The product B particles are absent. The activation energy is $E_a=100$ and the reaction probability $P=0.1$. (a) Prediction of Eq. (110) coupled to the Eulerian self-similar solutions (76)–(78). We notice the steep increase of c_B due to the discontinuous shock front. (b) Results of the integration of Eq. (110) coupled to the Navier-Stokes equations. Here, we notice that the increase of c_B is not so steep as in (a) because of the effect of the width of the shock front. Moreover, c_B increases slightly faster behind the shock than in (a) because of the heating due to the viscosities and heat conductivity. (c) Results of the molecular dynamics simulations. The macrofield c_B is obtained by averaging in concentric annuli of width $\Delta r=5$ over the $10N=101\ 350$ hard disks in 10 runs from random initial conditions. We notice the nice agreement with (b). The units are set by taking hard disks of unit mass and diameter and $k_B=1$.

coefficients are important for long-time relaxations and can thus be neglected in the description of a finite-time blowup phenomenon such as the shock-wave implosion.

The main purpose of the present paper has been to investigate the maximum temperature reached at the implosion of the shock wave in the center of the contracting cavity. The Eulerian description predicts a singularity in the temperature macrofield resulting in an infinite maximum temperature at the implosion, which is unphysical. In reality, the fact that the fluid is composed of particles and is, thus, affected by molecular fluctuations leads to dissipative effects, such as the shear and bulk viscosities as well as the heat conductivity, which precludes such a singularity in the temperature. It is for a similar reason that the shock wave has a smooth front with a width of the order of the mean free path, instead of presenting a discontinuity as described by the nondissipative Euler equations. Actually, the results of the integration of the Navier-Stokes equations, which incorporate the effects of the viscosities and heat conductivity, are in excellent agreement with the molecular dynamics simulations as well as the Enskog DSMC results. This agreement shows that the dissipation due to the shear and bulk viscosities and the heat conductivity is responsible for (i) the nonvanishing width of the shock front, (ii) the heating proceeding behind the shock front, and (iii) the finite maximum value of the central temperature at the instant of the shock-wave implosion.

Nevertheless, these dissipative effects manifest themselves on top of the profiles of the macrofields predicted by the self-similar solutions of Euler's equations, which are thus smoothed out by the dissipative effects on the spatial scale of the mean free path. The self-similar solutions obey a scaling law with an exponent α depending on the system dimension, on the equations of state of the fluid, and in the case of a nonpolytropic fluid such as the hard-disk fluid, on the density of the fluid before the shock front. This scaling exponent given by the theory of the self-similar solutions is remarkably well confirmed by the MD and Enskog DSMC simulations, as well as by the Navier-Stokes calculations. The increase of temperature at the shock-wave implosion can therefore be very well described by the Eulerian self-similar solutions on spatial scales larger than the mean free path. However, we have to suppose that the infinite singularity of the temperature predicted by Euler's equations is smoothed out on a dissipative length scale of the order of the mean free path. These considerations have led us to derive an analytic expression for the maximum temperature in Sec. III F for $D=2$ and in the Appendix for $D=3$. This analytic expression for the maximum temperature provides us with a comprehensive scheme for understanding the results of the MD and Enskog DSMC simulations, as well as of the Navier-Stokes calculations. A good agreement is found for the dependence of the maximum temperature on the mass of the particles and the speed of the wall of the contracting cavity, as well as on its initial radius in the supersonic regime.

In the subsonic regime, a wave also propagates from the moving wall to the center but its width is much broader than in the supersonic regime so that it cannot be considered as a shock wave. As the wall speed c increases the width of the wave front decreases and tends to a value of the order of the mean free path, while the maximum temperature increases as

the square of the wall speed c . In the supersonic regime, the maximum temperature can be analytically derived from the Eulerian self-similar solutions, which describe in detail how the energy is focused to the center of the contracting cavity. The dependence of the maximum temperature on the wall speed and on the mass of the particles can be predicted by a simple dimensional analysis. However, the dependence on the initial radius R_0 of the contracting cavity is very nontrivial because it involves the exponent α of the self-similar solutions.

The implosion of the shock wave is a very fast process on a time scale over which the dissipative effects have no time to manifest themselves on spatial scales larger than the mean free path. A consequence is that the large gradients of temperature in the process have negligible effects on a mixture of particles of different masses on the time scale of the implosion. The ratio of concentrations of species of different masses thus remains essentially constant, as predicted by the nondissipative Eulerian description and confirmed by molecular dynamics simulations.

Besides, we have also studied the effects of the shock wave on a simple reaction which is passively driven by the hydrodynamics. It is an isoenergetic isomerization $A \rightleftharpoons B$ with a given activation energy. This reaction is simple enough that its reaction rate can be analytically derived from Enskog's kinetic theory for a dense fluid. This reaction rate is very well verified by molecular dynamics simulations in a fluid at rest. In the contracting cavity, the reaction is observed to be induced by (i) the heating due to the passage of the shock wave which provides the main contribution to the product B , and (ii) the heating by the viscosities and the heat conductivity behind the shock which contribute to a small amount. The concentration profiles of the product B are very well described by the Navier-Stokes equations coupled to the reaction equation for the concentration difference between the reactive species A and B .

Recently, it has been noted that the applicability of the coupled Navier-Stokes equations (92)–(94) and reaction equation (110) is limited to systems in which the time scale of the chemical reactions is neither too slow nor too large relative to the hydrodynamic time scales [18]. The hydrodynamic time scales are those related to sound propagation and to dissipation. Near a shock, the hydrodynamic gradients become of order one over a distance of the mean free path so that the hydrodynamic time scales are comparable to the mean free time. On the other hand, when the temperature is comparable to, or larger than, the energy barrier for chemical reactions, the time scale of the chemical reactions becomes the mean free time multiplied by the reaction probability and the latter is finite if the concentrations are not near their equilibrium values. The conclusion is that if the concentrations are not near their equilibrium values and the temperature is not small compared to the reaction energy barrier, then (a) near a shock, the chemical time scale is likely to be comparable to the hydrodynamic time scales, and (b) away from a shock, the chemical time scales are likely to be much shorter than the hydrodynamic time scales. Case (a) corresponds to what are termed in Ref. [18] as “slow” or “moderate” reactions, for which the phenomenological description, or some small generalization thereof, is applicable.

Case (b) corresponds to “fast” reactions for which the phenomenological description is likely to be invalid. However, for the system studied in the present paper, case (b) may never occur as the chemical reaction exhausts itself during the period of shock focusing, when the system is still described by case (a), thus explaining the good agreement between theory and simulation.

In conclusion, the main features of an imploding shock wave can be described in terms of the Eulerian self-similar solutions considering the dissipative effects of the viscosities and the heat conductivity on the length scale of the mean free path. These considerations provide us with an analytic expression for the maximum temperature reached at the implosion.

ACKNOWLEDGMENTS

The authors thank Professor J.-P. Boon and Professor G. Nicolis for support and encouragement in this research, and Dr. I. Claus for assistance in the development of one of the codes. The ULB is thanked for financial support. P.G. is grateful to the FNRS Belgium for financial support.

APPENDIX: MAXIMUM TEMPERATURE IN THREE DIMENSIONS

In a three-dimensional (3D) hard-sphere fluid, the equation of state of the scaled-particle theory is given by [12]

$$p(T, n) = nk_B T f(y), \quad (\text{A1})$$

where

$$f(y) = \frac{1 + y + y^2}{(1 - y)^3}, \quad \text{with } y = \frac{4\pi}{3} n a^3 \quad (D=3). \quad (\text{A2})$$

The Enskog factor is obtained as

$$Y(y) = \frac{f(y) - 1}{4y}. \quad (\text{A3})$$

The mean free path is thus estimated to be

$$\ell(n) \approx \frac{1}{4\sqrt{2}\pi a^2 n Y\left(\frac{4\pi}{3} a^3 n\right)} \quad (D=3). \quad (\text{A4})$$

The temperature profile at the instant of the implosion of the shock wave is again given by Eq. (88) so that, by a reasoning similar to the one in Sec. III F, the maximum temperature at the center of the cavity is given in $D=3$ by

$$k_B T_{\max} \approx mc^2 \frac{K_Z}{\gamma V(1)^2 f\left(\frac{4\pi}{3} a^3 n_0 G(\infty)\right)} \times \left\{ 4\sqrt{2}\pi a^2 n_0 G(\infty) Y\left(\frac{4\pi}{3} a^3 n_0 G(\infty)\right) R_0 \right\}^{(2/\alpha)-2}, \quad (\text{A5})$$

with the 3D values of the quantities α , $V(1)$, $G(\infty)$, and K_Z . Therefore, the maximum temperature has properties similar as in $D=2$.

-
- [1] W. Lauterborn, T. Kurz, R. Mettin, and C. D. Ohl, *Adv. Chem. Phys.* **110**, 295 (1999).
 [2] M. P. Brenner, S. Hilgenfeldt, and D. Lohse, *Rev. Mod. Phys.* **74**, 425 (2002).
 [3] C. C. Wu and P. H. Roberts, *Phys. Rev. Lett.* **70**, 3424 (1993).
 [4] V. Q. Vuong and A. J. Szeri, *Phys. Fluids* **8**, 2354 (1996).
 [5] B. D. Storey and A. J. Szeri, *Proc. R. Soc. London, Ser. A* **456**, 1685 (2000).
 [6] B. Metten, Ph.D. dissertation, Der Andere Verlag, Göttingen, 2001.
 [7] S. J. Ruuth, S. Putterman, and B. Merriman, *Phys. Rev. E* **66**, 036310 (2002).
 [8] H. Lin, B. D. Storey, and A. J. Szeri, *J. Fluid Mech.* **452**, 145 (2002).
 [9] M.-C. Chu, *Phys. Rev. Lett.* **76**, 4632 (1996).
 [10] L. Yuan, H. Y. Cheng, M.-C. Chu, and P. T. Leung, *Phys. Rev. E* **57**, 4265 (1998).
 [11] H. Y. Cheng, M.-C. Chu, P. T. Leung, and L. Yuan, *Phys. Rev. E* **58**, R2705 (1998).
 [12] J. A. Barker and D. Henderson, *Rev. Mod. Phys.* **48**, 587 (1976).
 [13] D. M. Gass, *J. Chem. Phys.* **54**, 1898 (1971).
 [14] S. Chapman and T. G. Cowling, *The Mathematical Theory of Non-uniform Gases* (Cambridge University Press, Cambridge, UK, 1960).
 [15] L. Landau and E. Lifchitz, *Mécanique des Fluides* (Editions MIR, Moscou, 1989).
 [16] Ya. B. Zel'dovich and Yu. P. Raizer, *Physics of Shock Waves and High-Temperature Hydrodynamic Phenomena* (Dover, New York, 2002).
 [17] J. M. Montanero and A. Santos, *Phys. Rev. E* **54**, 438 (1996).
 [18] J. F. Lutsko, *J. Chem. Phys.* **120**, 6325 (2004).